Two-step Synthesis of Hard Carbons Anode Material from Poplar Wood with Enhanced Performance for Sodium-Ion Batteries

Xiaojing Jiang,[a] Kai Zhou,[b] Jun Liang,[a] Zhulin Li,[a] Yujie Zhang,[a] Zhaojiang Wang [iD],[a,*] and Ligang Gai [iD] [b,*]

Hard carbon (HC) is regarded as the most prospective anode material for sodium-ion batteries. Biomass HC is favored due to the advantages of being inexpensive and easily available. Herein, hydrothermal treatment of poplar lateral branches at 220 °C for 4 h was employed as the first synthesis step for HC precursor with yield of 48.5%. The obtained precursor was subjected to the second step of carbonization under nitrogen atmosphere at 1200 °C, 1400 °C, and 1600 °C for synthesis of HC anode materials. Advantages of two step synthesis were confirmed in terms of inorganic impurities elimination, HC yield, and electrochemical performance. Inorganic impurities reduced from 0.46% in poplar wood to 0.26% in precursor. The HC yield was 34.6% for precursor from hydrothermal treatment of poplar wood, which was much higher than HC yield of 18.5% from direct carbonization of poplar wood. The obtained HC anode materials manifested high capacity, strong rate performance, and long-term stability for sodium-ion batteries as indicated by the capacity of 333 mA h g^{-1} at 0.1 C and 285 mA h g^{-1} at 2 C, and capacity retention of 92.9% after 200 cycles at 1 C. This research provides an eco-friendly approach for the high-value utilization of woody biomass as anode material for sodium-ion batteries.

INTRODUCTION

With the increasing depletion of fossil fuels, the most widely used energy source, and the growing environmental concerns associated with fossil fuel combustion, the need for efficient energy storage systems is growing. Based on this, the new energy industry is constantly developing, and the application of lithium-ion batteries (LIBs) is becoming increasingly widespread (Yunming *et al.* 2016; Xiao *et al.* 2017). However, the global reserves of lithium resources are limited, where 70% of them are distributed in the South American region, greatly limiting the development of LIBs. The sodium resource is found in the Earth's crust at a higher abundance of 2.75%, which was over 400 times greater than the abundance of the lithium resource (Yabuuchi *et al.* 2014; Kundu *et al.* 2015). At the

same time, sodium and lithium are elements belonging to group IA alkali metals, exhibiting comparable chemical characteristics. Sodium-ion batteries (SIBs) work on the similar principle as LIBs, relying on the "rocking chair" movement of metal ions between the anode and the cathode. Therefore, SIBs are considered a strong contender for the next generation of energy storage (Wang *et al.* 2018). But a well-known fact is that Na is much heavier than Li, so SIBs may not be suitable for transportation power. On the contrary, cheaper but heavier SIBs may be the preferred choice for fixed site energy storage.

The radius of the sodium ion is 0.026 nm, which is greater than that of the lithium ion. The common graphite anodes applied in LIBs are not suitable for SIBs (Ge and Fouletier 1988; Doeff *et al.* 1994; Cao *et al.* 2012). Currently, the anode materials for SIBs are mainly restricted to metals and amorphous carbons. Metal anodes have high initial capacities while the volume changes greatly during charging and discharging, resulting in safety concerns and inferior cycling performance (Li *et al.* 2018). Amorphous carbons are categorized into soft carbon and hard carbon. The crystal structure of soft carbons is more similar to graphite, which has high electrical conductivity but low initial Coulombic efficiency. The molecular-level structure of hard carbon is more intricate in comparison to the well-organized layer structure found in graphite (Xiao *et al.* 2016; Qiu *et al.* 2017b; Lu *et al.* 2018; Mittal *et al.* 2022; Tan *et al.* 2023). In 2012, Cao *et al.* (2012) found that the energy consumption of Na^+ insertion decreases as the interlayer distance of NaC_6 increases. This result consolidates that the larger interlayer spacing and short-range orderly structure of hard carbon is more favorable for Na^+ de/intercalation, and thus hard carbon is regarded as promising anode materials for SIBs.

Sony used hard carbon obtained from poly furfuryl alcohol for the first time as an anode material in 1991, marking the beginning of the industrialization of hard carbon. Recently, biomass-based hard carbon has garnered significant interest because of their renewability, environmental friendliness, and excellent electrochemical properties as anode materials for SIBs. Gaddam *et al.* (2017) mixed mango feedstock as a precursor with sulfuric acid solution and reacted it in an autoclave at 170 °C for 25 h, followed by high-temperature carbonization to obtain hard carbon materials. After undergoing 1,000 cycles at a high current density of 1 A g^{-1}, the material exhibited a capacity of 113 mA h g^{-1}. Li *et al.* (2015) synthesized monodisperse hard carbon spheres from sucrose, and the assembled battery exhibited the highest capacity of 220 mA h g^{-1} at 1600 °C. Zheng *et al.* (2019) used a one-step pyrolysis method to prepare poplar wood as hard carbon, which had a capacity of 330 mA h g^{-1} at 1 C and decayed to below 100 mA h g^{-1} at 2 C. Yu *et al.* (2018) immersed old loofahs in $ZnCl_2$ solution for 24 h and then carbonized them at 800 °C in a tube furnace to obtain loofah hard carbon, and the assembled batteries also had excellent cycling performance at 1000 mA g^{-1}. Rybarcyzk *et al.* (2019) directly carbonized rice husks and achieved a maximum battery capacity of 276 mA h g^{-1} at 1600 °C.

As a productive species, poplar trees are fast-growing and widely planted in the world, making it a rich resource for furniture and construction. However, the utilization rate of poplar side branches is extremely low, and are usually burnt after pruning. To realize the high-value utilization of poplar waste lateral branches, this work employs poplar waste lateral branches to prepare HC precursor by hydrothermal treatment. The obtained precursor was subjected to carbonization under argon flow at 1200 °C, 1400 °C, and 1600 °C for synthesis of HC anode materials. The electrochemical performance of poplar wood-derived HC anode materials were systematically evaluated.

EXPERIMENTAL

Materials

Poplar waste lateral branches were obtained from a forest farm in Shandong Province. The button cells (CR2032), Super P, and polyvinylidene fluoride (PVDF, Solvay 5130) were obtained from Zhengzhou Jinghong New Energy Technology Co., Ltd. (Henan, China). *N–methyl–2–pyrrolidinone* (NMP) was procured from Macklin Biochemical Technology Co., Ltd. (Shanghai, China).

HC Synthesis

Poplar wood chips were washed by water and then dried in an oven at 105 °C. Oven-dried poplar wood (10 g) and deionized water (150 mL) were placed in a 500-mL stainless pressure vessel of Series 4560 Parr reactor (Parr Instrument Company, Moline, IL, USA) and exposed to hydrothermal treatment at 220 °C for 4 h. Wood residue after hydrothermal treatment, known as HC precursor, was separated from liquid by filtration, and then dried in blast drying oven at 105 °C. The oven-dried precursor was placed in a planetary ball mill for size reduction at 300 RPM for 6 h. The ball-milled HC precursor was carbonized under N_2 of 0.5 L/min atmosphere at 1200 °C, 1400 °C, and 1600 °C for 3 h in a SK-06163 tube furnace (Tianjin Zhonghuan furnace Co., Ltd.). The obtained HC was denoted as HC-x, such as HC-1200, HC-1400, and HC-1600, where x represents the carbonization temperature.

Physicochemical Characterization

Ash content was used to quantified inorganic impurities in poplar wood and HC precursor, according to ISO 9087 (1998). The microstructure of HC-x was analyzed by SmartLab SE X-ray diffractometer (Rigaku Corporation, Tokyo, Japan) equipped with Cu Kα rays, and a scanning range of 5° to 85° at 20°/min. Scanning electron microscope (SEM) images of poplar wood and HC materials were captured using a Regulus SU8220 (Hitachi, Tokyo, Japan). X-ray photoelectron spectroscopy (XPS) analyses performed on HC materials were conducted on monochromatic Al K_α radiation using an ESCALAB QXi X-ray photoelectron spectrometer (Thermo Fisher Scientific, Waltham, MA, USA).

Electrochemical Measurement

The electrode paste was made by blending HC, conductive additive (Super P), and polyvinylidene fluoride (PVDF) binder in a mass ratio of 8:1:1 in *N–methyl–2–pyrrolidinone* (NMP) solvent. The mixture was then applied onto copper foil, and then vacuum dried at 120 °C for 12 h. The CR2032 button half-cell was assembled in a glove box filled with Ar atmosphere containing less than 10 ppm of both oxygen and moisture, with Na metal as the opposing electrode, Celgard® 2400 monolayer polypropylene membrane as the diaphragm, $NaPF_6$ 1.0 M in diethylene glycol dimethyl ether (DEGDME) as the electrolyte. Cyclic voltammograms (CVs) and electrochemical impedance spectra (EIS) were evaluated using CHI760E electrochemical workstation (CH Instruments, Shanghai, China). The CVs were measured with a sweep rate of 0.05 mV/s and a potential window of 0.01 V to 3.0 V. The EIS was recorded at an amplitude of 5 mV and frequencies spanning from 1 Hz to 10^5 Hz. The rate test was conducted using LANHE CT2001A battery tester (Wuhan Landian Co., China) with a potential window of 0.01 V to 2.8 V, and charging/discharging currents of 0.1 C, 0.2 C, 0.5 C, 1 C, and 2 C. The
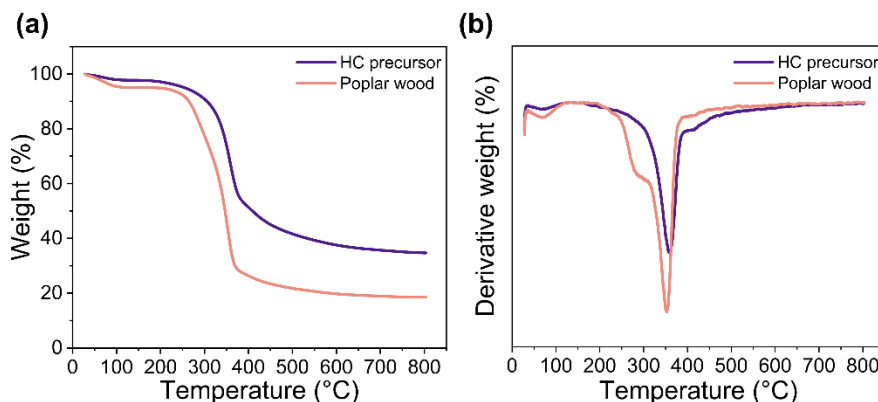
electrochemical performance of all batteries were evaluated on the mass basis of active materials on one electrode.

RESULTS AND DISCUSSION

Characterization of HC Precursor

Poplar wood chips were hydrothermally treated to obtain precursors of wood-based HC. In this process, poplar wood chips and water were placed in a high-temperature, high-pressure vessel and reacted for 4 h at 220 °C. The HC yield was 48.5% from hydrothermal treatment. The inorganic impurities in poplar wood chips and HC precursor were quantified in terms of ash content. The ash content was reduced from 0.4654% of poplar wood to 0.2607% of HC precursor. Through calculation, it was determined that the elimination of inorganic impurities from the wood chips during the hydrothermal treatment was 72.8%. Adrian Beda *et al.* (2020) examined the impact of inorganic impurities present in biomass on the characteristics of hard carbon and their subsequent electrochemical performance. It was found that the removal of crystalline inorganic impurities (K, Ca, Si, and Mg-based compounds), which was helpful for the increase of carbon content and electronic conductivity.

Thermogravimetric analysis (TGA) was used to assess the thermal stability of poplar wood and HC precursor. Both TGA and differential thermogravimetric (DTG) curves of poplar wood and HC precursor are shown in Fig. 1. Three regions of weight loss were observed in the TGA curves. The rapid weight loss at 250 °C to 400 °C is primarily due to the pyrolysis of hemicellulose and cellulose and the consequent release of oxygen-containing volatile substances (Velázquez Martí *et al.* 2023). The weight loss after 400 °C results from the release of CO and CO_2 from lignin and aromatic carbon through thermal degradation (Skreiberg *et al.* 2011; Gao *et al.* 2023; Velázquez Martí *et al.* 2023). From Table 2, the initial degradation temperature, which was defined as temperature corresponding to 5% weight loss, was 254.4 °C for HC precursor, which was higher than 175.1 °C for poplar wood. From DTG curves in Fig. 1b, HC precursor showed T_{max} (temperature at the maximum degradation rate) 359.8 °C, slightly higher than T_{max} 353.0 °C of poplar wood. This indicates the improvement of thermal stability of HC as result of hydrothermal treatment. The residual weight at 800 °C was 34.7% for HC precursor, much higher than 18.5% for poplar wood. These values are consistent to HC yield because weight keeps constant at higher temperature.

Fig. 1. (a) TGA curves of poplar wood and HC precursor, (b) DTG curves of poplar wood and HC precursor

Table 1. Characteristic Parameters of Poplar Wood and HC Precursor Determined by TGA

Samples	$T_{5\%}$[a] (°C)	$T_{10\%}$[b] (°C)	T_{max}[c] (°C)	Residue Weight (%)
Poplar wood	175.1	264.6	353.0	18.5
HC precursor	254.4	305.7	359.8	34.7

[a]$T_{5\%}$ is defined as the initial degradation temperature at 5% weight loss;
[b]$T_{10\%}$ is the degradation temperature at 10% weight loss;
[c]T_{max} is the temperature at the maximum degradation rate

Physicochemical Characterization of HC

Scanning electron microscopy was employed to observe the morphology of poplar wood and HC. As shown in Fig. 2, untreated poplar wood shows clear and organized xylem structure with smooth cell walls. The HC exhibited granular sedimentary morphology. HC materials from different carbonization temperatures are not distinguishable in morphology. The irregular granular morphology of HC was attributed to the precipitation of the liquefied wood during the hydrothermal process. These precipitates are very small in size, but aggregated together to form HC granules with average size of 15 μm. It is observed there are pores and channels within HC granules, which are believed to be favorable for the electrolyte penetration, and the embedding and detachment of Na^+.
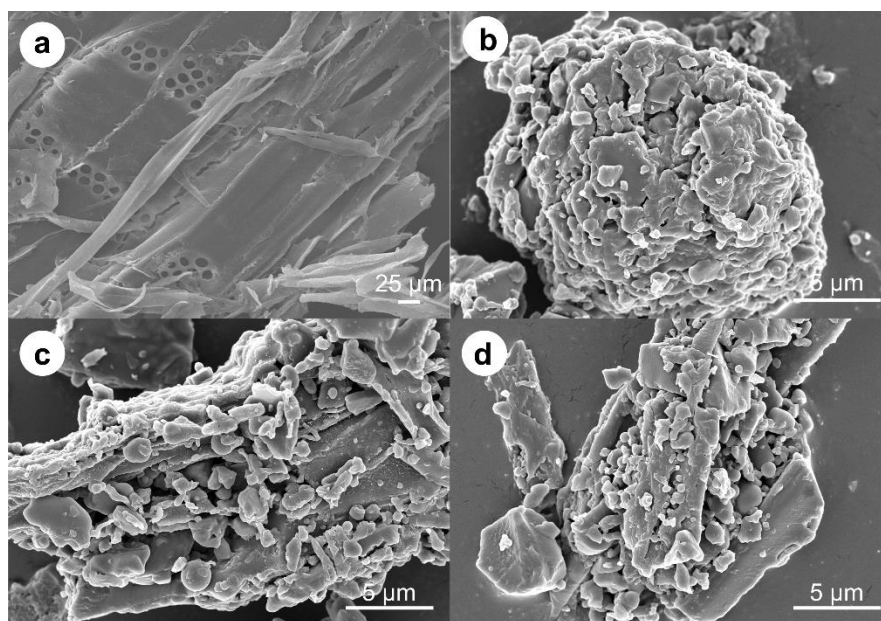

Fig. 2. SEM images of (a) poplar wood, (b) HC-1200, (c) HC-1400, and (d) HC-1600

Figure 3 shows XRD pattern and Raman spectra of HC. From Fig. 3a, two peaks in the XRD pattern represent the graphite (002) crystal plane and (100) crystal plane and appear at 23° and 43°, respectively. As the temperature for carbonization increased from 1200 °C to 1600 °C, both peaks showed tendency of being narrow and sharp. It shows that the crystallinity and graphitization of HC were enhanced with the increase of carbonization temperature. When the carbonization temperature was 1600 °C, the peak (002) shifted to a higher angle. This suggests that the local structural development of HC tends to be short-range ordered. In addition, no impurity peaks were detected in the XRD pattern, which

indicated that the impurities in the precursor are removed during the hydrothermal process. Based on the XRD pattern, structural parameters, such as d_{002}, La, Lc (González *et al.* 2004), and N (Qiu *et al.* 2017a) of HC were calculated with reference to Scherrer formula as descripted by Eqs. 1 through 4; where λ is the wavelength of the Cu K$_\alpha$ radiation, and K = 0.89. The equations are as follows:

$$d_{002} = \frac{\lambda}{2\sin\theta} \tag{1}$$

$$La = \frac{k\lambda}{\beta\sin\theta} \tag{2}$$

(β is the half peak width of (002))

$$Lc = \frac{k\lambda}{\beta\sin\theta} \tag{3}$$

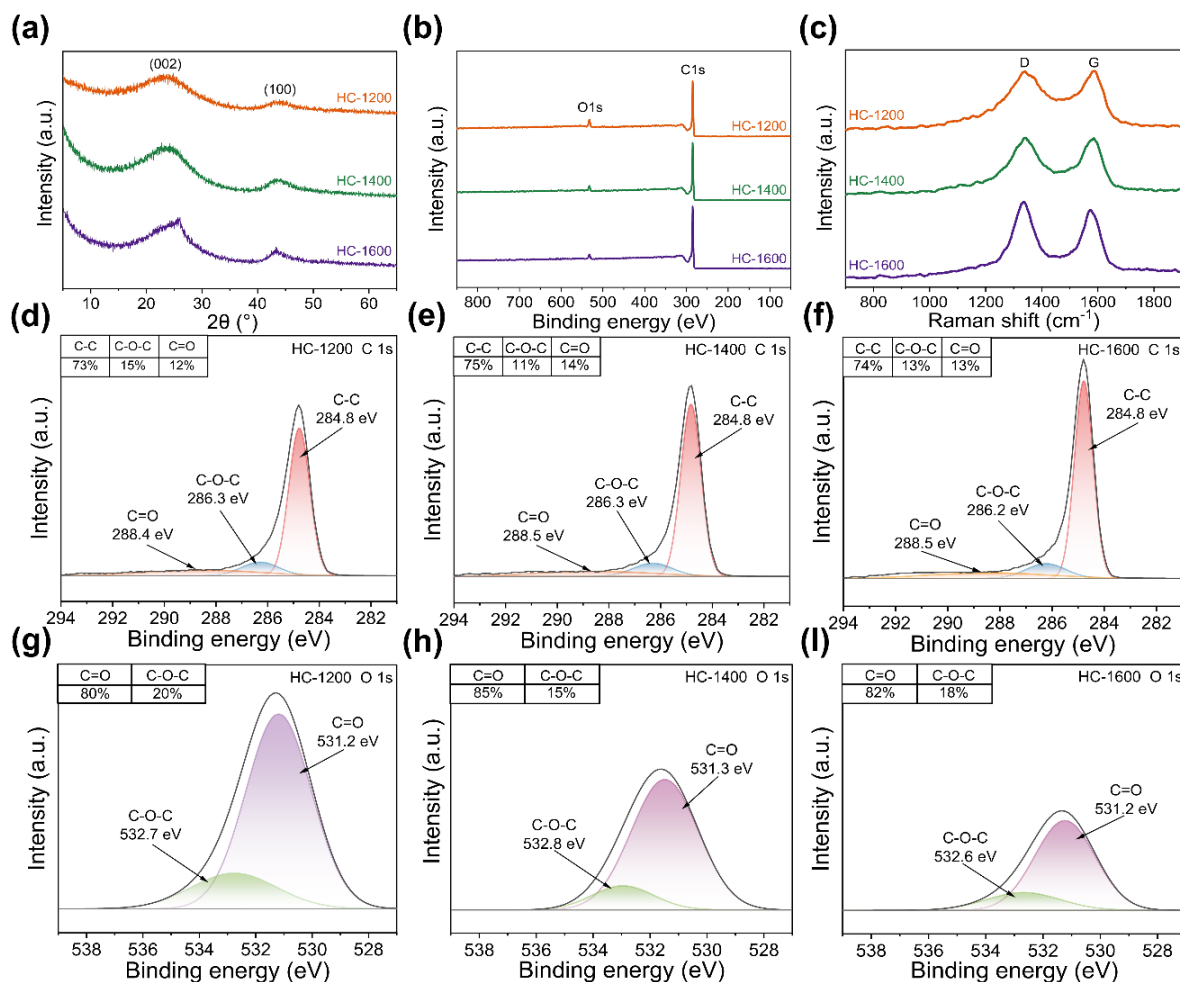(β is the half peak width of (100))

$$N = \frac{Lc}{d_{002}} \tag{4}$$

As illustrated in Table 2, the graphite-like layer spacing (d_{002}) was 0.381 nm at a carbonization temperature of 1200 °C. When the carbonization temperature was increased to 1600 °C, the d_{002} decreased to 0.371 nm. The d_{002} of all HC is greater than the critical minimum spacing (0.37 nm) for the insertion of Na$^+$ between graphite layers (Cao *et al.* 2012), and bigger than the d_{002} of standard graphene layers (0.335 nm)(Katzen *et al.* 2018). While the carbonization temperature increased, the average length of graphite-like microcrystal (La), the thickness of graphite-like microcrystal (Lc), and average number of graphene layer (N) increased from 4.24 nm, 0.87 nm, and 2.28 to 4.94 nm, 1.07 nm, and 2.93, respectively. The increase of d_{002} encouraged more Na$^+$ to be embedded, but too long La prevented Na$^+$ diffusion. Electrochemical test results also confirmed this finding.

The XPS was performed to obtain the elemental composition and bonding of HC. The XPS spectrum of HC (Fig. 3b) showed two peaks at 284.8 eV and 531.3 eV, corresponding to C 1s and O 1s, respectively. There were no peaks for K (around 300 eV), Si (around 100 eV), *etc.* in wood. It showed that HC after hydrothermal treatment had minimal impurities and was below the detection limit of XPS. The amount of carbon was 91.8 at% for HC-1200, 93.5 at% for HC-1400, and 94.4 at% for HC-1600. The XPS spectrum of C 1s was divided into three peaks (Fig. 3 d through f). The main peak at 284.8 eV corresponds to the sp^2-hybridization C–C (Wei *et al.* 2009). The peaks at 286.3 eV and 288.5 eV correspond to C–O–C and C=O groups, respectively (Ou *et al.* 2015). The two peaks of O 1s at 531.2 eV and 532.6 eV correspond to C=O and C–O–C, respectively (Ou *et al.* 2015; Zizhang *et al.* 2017). The oxygen was mainly derived from heat-stable groups in carbon and small amounts of oxygen and water adsorbed on the surface. Several studies have shown that the surface redox reaction of C=O with Na$^+$ enhances Na$^+$ storage (Kim *et al.* 2013; Shao *et al.* 2013; Kim *et al.* 2014; Liu *et al.* 2016). The reversible reaction can be expressed by Eq. 5:

$$-C-O-Na \leftrightarrow -C=O + Na^+ + e \tag{5}$$

Looking at the percentage in C 1s and O 1s plots, HC-1400 has the highest percentage of C=O, 14% and 85%, respectively. It was consistent with the results in the rate plots where the HC-1400 has the highest capacity.

Raman spectrograms of HC showed distinct D and G peaks at ~1338 cm^{-1} and ~1586 cm^{-1}, respectively, both attributed to the sp^2 site. The D peak represents the atomic pattern of sp^2 in the carbon ring (Ferrari and Basko 2013). There is no D peak without the ring structure. The G peak represents the oscillation of all sp^2 atoms in the carbocyclic or carbon chain (Ferrari *et al.* 2004). The integral area ratio of the G peak to the D peak (I_G/I_D) represents the defect concentration of the graphitic material, where an increase in the integral intensity ratio corresponds to a decrease in defect concentration and an increase in ordering (Andrea *et al.* 2004). From Table 2, it is shown that the I_G/I_D increased from 0.48 to 0.77 when the carbonization temperature was increased from 1200 °C to 1600 °C. It indicated that the orderliness of HC increases along with the carbonization temperatures, which was consistent with the tendency to short-range orderliness in XRD (Fig. 3a).

Fig. 3. (a) XRD pattern, (b) XPS spectra, (c) Raman spectra, (d through f) C 1s, and (g through i) O 1s of HC materials from different carbonization temperatures

Table 2. Structure Features of HC Materials from XRD Pattern and Raman Spectra

Sample Label	d_{002} (nm)	Lc^1 (nm)	La^2 (nm)	N^3	I_G/I_D^4
HC-1200	0.381	0.87	4.24	2.28	0.48
HC-1400	0.376	0.92	4.39	2.44	0.61
HC-1600	0.371	1.07	4.94	2.93	0.77

[1] Lc is the thickness of graphite-like microcrystals;
[2] La is the average length of graphite-like microcrystals;
[3] N is the average number of graphite-like microcrystalline layers;
[4] I_G/I_D is the integral intensity ratio of the G peak to the D peak
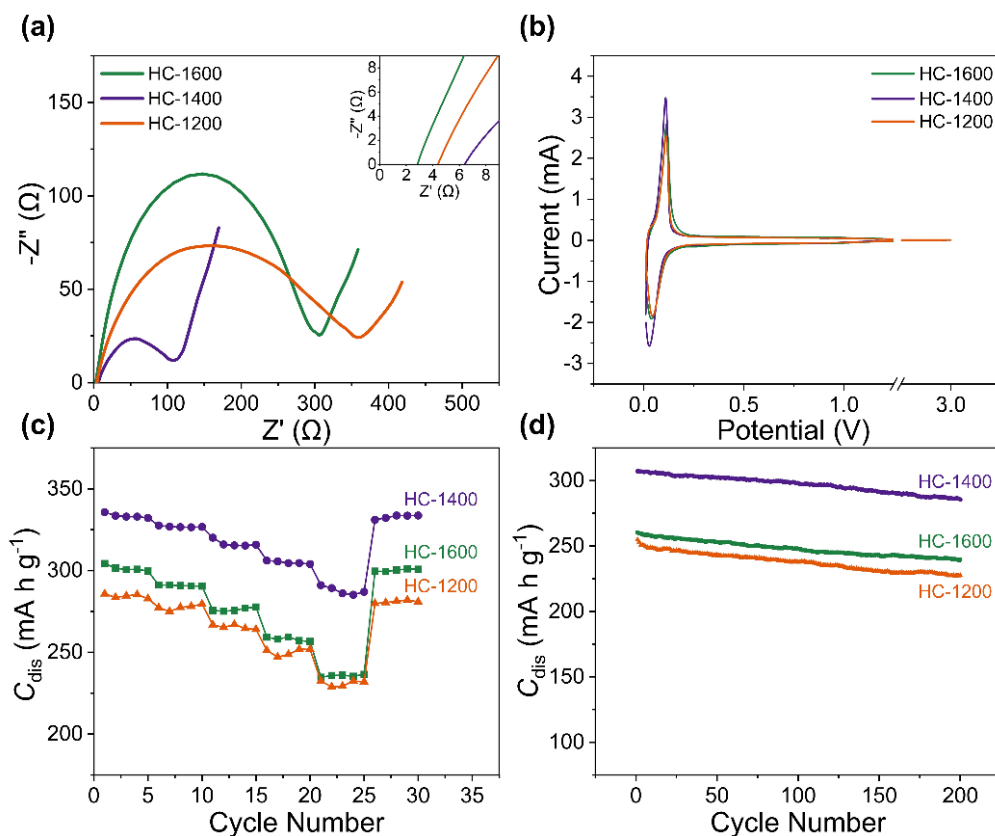
Electrochemical Performance of HC

The electrode kinetics of HC as anode for sodium-ion batteries were evaluated by electrochemical impedance spectra (EIS) at amplitudes of 5 mV and frequencies ranging from 1 Hz to 10^5 Hz. As shown in Fig. 4a, EIS consists of plotting so-called Nyquist plots, which are composed of a semicircle in the high-frequency region and a short slanting line in the low-frequency region. The diameters of the semicircle in the Nyquist plot usually correspond to the charge transfer resistance (Rct). An increase in the diameter of the semicircle indicates a slowing down of the electrochemical reaction at the electrode surface. From Fig. 4a, HC-1400 sodium battery showed the lowest charge transfer resistance, while HC-1200 sodium battery showed the highest charge transfer resistance. The Warburg slope line represents the diffusion capacity of sodium ions in the electrode, with a greater slope indicating a higher ion transport capacity (Moss *et al.* 2009; Nunes *et al.* 2024). Figure 4a shows the HC-1400 had the highest slope, which indicated the fastest electrochemical reaction on the surface and the strongest ion transport capacity. It was consistent with the rate plots.

Figure 4b shows the cyclic voltammogram (CV) of the HC anode of SIBs in the voltage range of 0 to 3 V. The shape of CV deviates to some extent from 'duck' shape. It was observed from the Fig. 4b that the CV curves were smooth, which proved that the HC material was stable and had no extra reactions. The nice symmetry of the redox peaks in the figure also proved the high reversibility of the electrode reaction. During the positive scanning, an oxidation peak was observed around 0.1 V, corresponding to the removal of Na^+ from HC. The sharp reduction peak around 0.03 V observed in the negative scanning corresponds to the insertion of Na^+ into HC (Wang *et al.* 2013). The oxidation peaks and reduction peak showed a tendency of strengthening and then weakening with the increase of carbonization temperature, which was highly consistent with the rate plots.

Figure 4c shows a rate plot where the reversible capacity of HC can be observed, with a potential window of 0.01 V to 2.8 V and charging/discharging currents of 0.1 C, 0.2 C, 0.5 C, 1 C, and 2 C (1 C = 372 mA h g^{-1}). HC-1400 electrode showed the best electrochemical performance, which reversible capacity attained 333 mA h g^{-1} at 0.1 C and 285 mA h g^{-1} at 2 C. The reversible capacity of HC-1200 and HC-1600 was 284 mA h g^{-1} and 300 mA h g^{-1} at 0.1 C, respectively. However, it was not distinguishable any more at 2 C, which is about 232 mA h g^{-1}. Satisfactorily, all HC samples were cycled 25 times at different current density and return to 0.1 C, the capacity could still be restored to the initial amount. The electrode cycling performance for 200 cycles at a current density of 1 C is shown in Fig. 4d. At the beginning of the cycle, the battery capacity of HC-1400 was 307
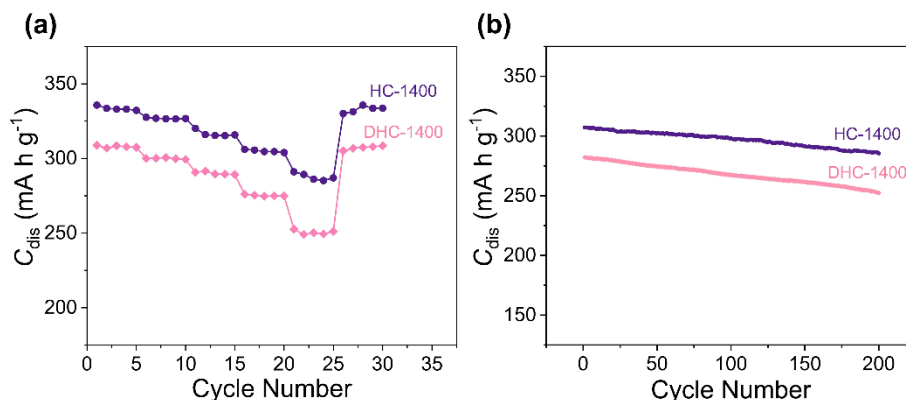
mA h g^{-1}. The battery capacity retained 92.9% after 200 cycles. This likewise occurred to HC-1200 and HC-1600 as indicated by the capacity retentions of 90.8% and 89.58%, respectively.

Fig. 4. Electrochemical performance of HC electrodes: (a) Nyquist plots, (b) CVs, (c) rate plots, and (d) Cycling plots

For comparison with HC-1400 from two-step synthesis, namely hydrothermal treatment of wood and carbonization at 1400 °C, hard carbon from direct carbonization at 1400 °C of wood was synthesized and named as DHC-1400. Figure 5 shows the comparison of the rate performance and cycling performance between HC-1400 and DHC-1400.

The capacities of HC-1400 and DHC-1400 electrodes at various rates (Fig. 5a) demonstrate superb rate capability 4 of HC-1400. The specific capacity of HC-1400 at current density of 0.1 C, 0.2 C, 0.5 C, 1 C, 2 C is 333, 326, 315, 305, 285 mA h g^{-1}, respectively. In comparison, DHC-1400 cannot deliver such a high capacity, especially at larger rates. From Fig. 5b, HC-1400 also offers a slightly higher in cycling stability at rate of 1 C over 200 cycles compared with DHC-1400. The capacity retention of DHC-1400 after 200 cycles was 89.3% , which is lower than 92.9% of HC-1400.

(a)   **(b)**

Fig. 5. (a) Rate performance of HC-1400 and DHC-1400 at various rates from 0.1 C to 2 C; (b) Cycling performance of HC-1400 and DHC-1400 at rate of 1 C

CONCLUSIONS

1. Hard carbons were obtained by hydrothermal treatment and subsequent carbonization at different pyrolysis temperatures from 1200 °C to 1600 °C. The layer spacing of the obtained hard carbons exceeded 0.37 nm, creating favorable conditions for the insertion/removal of Na^+.

2. The HC-1400 exhibited a maximum reversible capacity of 333 mA h g^{-1} at 0.1 C and maintained a reversible capacity of 285 mA h g^{-1} at high current density 2 C. It showed a capacity retention of 92.9% after 200 cycles at 1 C.

3. The synthesis of hard carbon from poplar wood offers promising opportunities for sodium-ion battery energy storage because of its cost-effectiveness, high capacity, excellent cycling stability, and efficient utilization of waste biomass.

ACKNOWLEDGMENTS

REFERENCES CITED

Beda, A., Le Meins, J.-M., Taberna, P.-L., Simon, P., and Matei Ghimbeu, C. (2020). "Impact of biomass inorganic impurities on hard carbon properties and performance in Na-ion batteries," *Sustainable Materials and Technologies* 26, Article ID e00227. DOI: 10.1016/j.susmat.2020.e00227

Cao, Y., Xiao, L., Sushko, M. L., Wang, W., Schwenzer, B., Xiao, J., Nie, Z., Saraf, L. V., Yang, Z., and Liu, J. (2012). "Sodium ion insertion in hollow carbon nanowires for battery applications," *Nano Letters* 12(7), 3783-3787. DOI: 10.1021/nl3016957

Doeff, M. M., Ma, Y., Visco, S. J., and de Jonghe, L. C. (1994). "Electrochemical insertion of sodium into carbon," *Journal of the Electrochemical Society* 140(12), Article Number L169. DOI: 10.1149/1.2221153

Ferrari, A. C., and Robertson, J. (2004). "Raman spectroscopy of amorphous, nanostructured, diamond–like carbon, and nanodiamond," *Philosophical Transactions of the Royal Society A: Mathematical Physical & Engineering Sciences* 362(1824), 2477-2512. DOI: 10.1098/rsta.2004.1452

Ferrari, A. C., and Basko, D. M. (2013). "Raman spectroscopy as a versatile tool for studying the properties of graphene," *Nature Nanotechnology* 8(4), 235-246. DOI: 10.1038/nnano.2013.46

Gaddam, R. R., Farokh Niaei, A. H., Hankel, M., Searles, D. J., Kumar, N. A., and Zhao, X. S. (2017). "Capacitance-enhanced sodium-ion storage in nitrogen-rich hard carbon." *Journal of Materials Chemistry A* 5(42), 22186-22192. DOI: 10.1039/c7ta06754b

Guo, Z., Zhang, X., Kang, Y., and Zhang, J. (2017). "Biomass-derived carbon sorbents for Cd(II) removal: Activation and adsorption mechanism," *ACS Sustainable Chemistry Engineering* 5(5), 4103-4109. DOI: 10.1021/acssuschemeng.7b00061

Gao, S., Chen, X., Tian, G., Fu, Y., Qin, M., and Wang, Z. (2023). "Preparation of light-colored bio-based particles by isocyanate-modified lignins and its application for tetracycline adsorption," *International Journal of Biological Macromolecules* 253, Article ID 127107. DOI: 10.1016/j.ijbiomac.2023.127107

Ge, P., and Fouletier, M. (1988). "Electrochemical intercalation of sodium in graphite," *Solid State Ionics* 28-30, 1172-1175. DOI: 10.1016/0167-2738(88)90351-7

González, D., Montes-Morán, M. A., Suárez-Ruiz, I., and Garcia, A. B. (2004). "Structural characterization of graphite materials prepared from anthracites of different characteristics: A comparative analysis," *Energy & Fuels* 18(2), 365-370. DOI: 10.1021/ef030144+

ISO 9087 (1998). "Wood determination of nail and screw holding power under axial load application," International Organization for Standardization, Geneva, Switzerland.

Katzen, J. M., Velický, M., Huang, Y., Drakeley, S., Hendren, W., Bowman, R. M., Cai, Q., Chen, Y., Li, L., and Huang, F. (2018). "rigorous and accurate contrast spectroscopy for ultimate thickness determination of micrometer-sized graphene on gold and molecular sensing," *ACS Applied Materials & Interfaces* 10(26), 22520-22528. DOI: 10.1021/acsami.8b01208

Kim, H., Lim, H.-D., Kim, S.-W., Hong, J., Seo, D.-H., Kim, D.-c., Jeon, S., Park, S., and Kang, K. (2013). "Scalable functionalized graphene nano-platelets as tunable cathodes for high-performance lithium rechargeable batteries," *Scientific Reports* 3(1), Article Number 1506. DOI: 10.1038/srep01506

Kim, H., Park, K.-Y., Hong, J., and Kang, K. (2014). "All-graphene-battery: Bridging the gap between supercapacitors and lithium ion batteries." *Scientific Reports* 4(1), Article ID 5278. DOI: 10.1038/srep05278

Kundu, D., Talaie, E., Duffort, V., and Nazar, L. F. (2015). "The emerging chemistry of sodium ion batteries for electrochemical energy storage," *Angewandte Chemie International Edition* 54(11), 3431-3448. DOI: 10.1002/anie.201410376

Li, Q., Jiang, K., Li, X., Qiao, Y., Zhang, X., He, P., Guo, S., and Zhou, H. (2018). "A high-crystalline $NaV_{1.25}Ti_{0.75}O_4$ anode for wide-temperature sodium-ion battery," *Advanced Energy Materials* 8(25), 1801162.1-1801162.7. DOI: 10.1002/aenm.201801162

Li, Y., Xu, S., Wu, X., Yu, J., Wang, Y., Hu, Y.-S., Li, H., Chen, L., and Huang, X. (2015). "Amorphous monodispersed hard carbon micro-spherules derived from biomass as a high performance negative electrode material for sodium-ion batteries," *Journal of Materials Chemistry A* 3(1), 71-77. DOI: 10.1039/c4ta05451b

Liu, C., Koyyalamudi, B. B., Li, L., Emani, S., Wang, C., and Shaw, L. L. (2016). "Improved capacitive energy storage via surface functionalization of activated carbon as cathodes for lithium ion capacitors," *Carbon* 109, 163-172. DOI: 10.1016/j.carbon.2016.07.071

Li, Y., Hu, Y.-S., Titirici, M.-M., Chen, L., Xuejie, and Huang, X. (2016). "hard carbon microtubes made from renewable cotton as high-performance anode material for sodium-ion batteries," *Advanced Energy Materials* 6(18), Article Number 1600659. DOI: 10.1002/aenm.201600659

Lu, P., Sun, Y., Xiang, H., Liang, X., and Yu, Y. (2018). "3D amorphous carbon with controlled porous and disordered structures as a high-rate anode material for sodium-ion batteries," *Advanced Energy Materials* 8(8), Article Number 1702434. DOI: 10.1002/aenm.201702434

Mittal, U., Djuandhi, L., Sharma, N., and Andersen, H. L. (2022). "Structure and function of hard carbon negative electrodes for sodium-ion batteries," *Journal of Physics: Energy* 4(4), Article ID 042001. DOI: 10.1088/2515-7655/ac8dc1

Moss, P. L., Au, G., Plichta, E. J., and Zheng, J. P. (2009). "Investigation of solid electrolyte interfacial layer development during continuous cycling using ac impedance spectra and micro-structural analysis," *Journal of Power Sources* 189(1), 66-71. DOI: 10.1016/j.jpowsour.2008.11.048

Nunes, H., Martinho, J., Fermeiro, J., Pombo, J., Mariano, S., and Calado, M. d. R. (2024). "Impedance analysis and parameter estimation of lithium-ion batteries using the EIS technique," *IEEE Transactions on Industry Applications* 60(3), 5048-5060. DOI: 10.1109/tia.2024.3365451

Ou, J., Zhang, Y., Chen, L., Zhao, Q., Meng, Y., Guo, Y., and Xiao, D. (2015). "Nitrogen-rich porous carbon derived from biomass as a high performance anode material for lithium ion batteries." *Journal of Materials Chemistry A* 3(12), 6534-6541. DOI: 10.1039/c4ta06614f

Qiu, S., Xiao, L., Sushko, M. L., Han, K. S., Shao, Y., Yan, M., Liang, X., Mai, L., Feng, J., Cao, Y., *et al*. (2017a). "Manipulating adsorption–insertion mechanisms in nanostructured carbon materials for high-efficiency sodium ion storage," *Advanced Energy Materials* 7(17), Article ID 1700403. DOI: 10.1002/aenm.201700403

Rybarczyk, M. K., Li, Y., Qiao, M., Hu, Y.-S., Titirici, M.-M., and Lieder, M. (2019). "Hard carbon derived from rice husk as low cost negative electrodes in Na-ion batteries," *Journal of Energy Chemistry* 29, 17-22. DOI: 10.1016/j.jechem.2018.01.025

Shao, Y., Xiao, J., Wang, W., Engelhard, M., Chen, X., Nie, Z., Gu, M., Saraf, L. V., Exarhos, G., Zhang, J.-G., *et al*. (2013). "Surface-driven sodium ion energy storage in nanocellular carbon foams," *Nano Letters* 13(8), 3909-3914. DOI: 10.1021/nl401995a

Skreiberg, A., Skreiberg, Ø., Sandquist, J., and Sørum, L. (2011). "TGA and macro-TGA characterisation of biomass fuels and fuel mixtures," *Fuel* 90(6), 2182-2197. DOI: 10.1016/j.fuel.2011.02.012

Tan, S., Yang, H., Zhang, Z., Xu, X., Xu, Y., Zhou, J., Zhou, X., Pan, Z., Rao, X., Gu, Y., *et al*. (2023). "The progress of hard carbon as an anode material in sodium-ion batteries," *Molecules* 28(7), Article Number 3134. DOI: 10.3390/molecules28073134

Velázquez Martí, B., Gaibor-Chavez, J., López Cortés, I., and Olivares Aguilar, L. E. (2023). "Evaluation of the intermediate values of the TGA curves as indicators of the proximal analysis of biomass," *Agronomy* 13(10), Article Number 2552. DOI: 10.3390/agronomy13102552

Wang, H. G., Wu, Z., Meng, F. L., Ma, D. L., Huang, X. L., Wang, L. M., and Zhang, X. B. (2013). "Nitrogen-doped porous carbon nanosheets as low-cost, high-performance anode material for sodium-ion batteries," *Chemsuschem* 6(1), 56-60. DOI: 10.1002/cssc.201200680

Wang, P. F., You, Y., Yin, Y. X., and Guo, Y. G. (2018). "layered oxide cathodes for sodium‐ion batteries: Phase transition, air stability, and performance," *Advanced Energy Materials* 8(8), Article ID 1701912. DOI: 10.1002/aenm.201701912

Wei, D., Liu, Y., Zhang, H., Huang, L., Wu, B., Chen, J., and Yu, G. (2009). "Scalable synthesis of few-layer graphene ribbons with controlled morphologies by a template method and their applications in nanoelectromechanical switches," *Journal of the American Chemical Society* 131(31), 11147-11154. DOI: 10.1021/ja903092k

Xiao, L., Cao, Y., Henderson, W. A., Sushko, M. L., Shao, Y., Xiao, J., Wang, W., Engelhard, M. H., Nie, Z., and Liu, J. (2016). "Hard carbon nanoparticles as high-capacity, high-stability anodic materials for Na-ion batteries," *Nano Energy* 19, 279-288. DOI: 10.1016/j.nanoen.2015.10.034

Xiao, Y., Zhu, Y., Gao, T., Zhong, B. H., and Guo, X. (2017). "LiNi$_{0.5}$Mn$_{1.5}$O$_4$ hollow nano-micro hierarchical microspheres as advanced cathode for lithium ion batteries," *Ionics* 23, 27-34. DOI: 10.1007/s11581-016-1804-0

Yabuuchi, N., Kubota, K., Dahbi, M., and Komaba, S. (2014). "Research development on sodium-ion batteries," *Chemical Reviews* 114(23), 11636-11682. DOI: 10.1021/cr500192f

Yu, C., Hou, H., Liu, X., Yao, Y., Liao, Q., Dai, Z., and Li, D. (2018). "Old-loofah-derived hard carbon for long cyclicity anode in sodium ion battery," *International Journal of Hydrogen Energy* 43(6), 3253-3260. DOI: 10.1016/j.ijhydene.2017.12.151

Zheng, Y., Lu, Y., Qi, X., Wang, Y., Mu, L., Li, Y., Ma, Q., Li, J., and Hu, Y.-S. (2019). "Superior electrochemical performance of sodium-ion full-cell using poplar wood derived hard carbon anode," *Energy Storage Materials* 18, 269-279. DOI: 10.1016/j.ensm.2018.09.002